

# Baroclinic geostrophic adjustment in a rotating circular basin

By GEOFFREY W. WAKE<sup>1</sup>, GREGORY N. IVEY<sup>1</sup>,  
JÖRG IMBERGER<sup>1</sup>, N. ROBB McDONALD<sup>2</sup>  
AND ROMAN STOCKER<sup>3</sup>

<sup>1</sup>Centre for Water Research, University of Western Australia, Nedlands,  
Western Australia 6907, Australia

<sup>2</sup>Department of Mathematics, University College London, London WC1E 6BT, UK

<sup>3</sup>Department of Applied Mathematics, Massachusetts Institute of Technology, Cambridge,  
MA 02139, USA

(Received 3 June 2003 and in revised form 27 April 2004)

Baroclinic geostrophic adjustment in a rotating circular basin is investigated in a laboratory study. The adjustment process consists of a linear phase before advective and dissipative effects dominate the response for longer time. This work describes in detail the hydrodynamics and energetics of the linear phase of the adjustment process of a two-layer fluid from an initial step height discontinuity in the density interface  $\Delta H$  to a final response consisting of both geostrophic and fluctuating components. For a forcing lengthscale  $r_f$  equal to the basin radius  $R_0$ , the geostrophic component takes the form of a basin-scale double gyre while the fluctuating component is composed of baroclinic Kelvin and Poincaré waves. The Burger number  $S = R/r_f$  ( $R$  is the baroclinic Rossby radius of deformation) and the dimensionless forcing amplitude  $\epsilon = \Delta H/H_1$  ( $H_1$  is the upper-layer depth) characterize the response of the adjustment process. In particular, comparisons between analytical solutions and laboratory measurements indicate that for time  $\tau$ :  $1 < \tau < S^{-1}$  ( $\tau$  is time scaled by the inertial period  $2\pi/f$ ), the basin-scale double gyre is established, followed by a period where the double gyre is sustained, given by  $S^{-1} < \tau < 2\epsilon^{-1}$  for a moderate forcing and  $S^{-1} < \tau < \tau_D$  for a weak forcing ( $\tau_D$  is the dimensionless dissipation timescale due to Ekman damping). The analytical solution is used to calculate the energetics of the baroclinic geostrophic adjustment. The results are found to compare well with previous studies with partitioning of energy between the geostrophic and fluctuating components exhibiting a strong dependence on  $S$ . Finally, the outcomes of this study are considered in terms of their application to lakes influenced by the rotation of the Earth.

---

## 1. Introduction

The seminal work on the geostrophic adjustment of a rotating fluid under the influence of gravity, in which the balance between horizontal pressure gradients and the Coriolis force is restored from an initially unbalanced state, was performed by Rossby (1937, 1938). Gill (1982) considered an infinite domain initially at rest with an initial step in the surface elevation and after linearizing under the assumption of small perturbations, was able to show that the establishment of geostrophic balance was made possible by the radiation of Poincaré waves away from an adjustment region of width equal to the Rossby radius of deformation  $R$ . Subsequent studies have focused on extending Gill's (1982) solution by considering the weakly nonlinear (Hermann,

Rhines & Johnson 1989) and fully nonlinear (Helfrich, Kuo & Pratt 1999) barotropic geostrophic adjustment in a rotating channel of infinite length. Hermann *et al.* (1989) proposed that a weakly nonlinear barotropic geostrophic adjustment in a rotating channel was separable into an initial linear phase followed by a nonlinear phase. During the linear phase, the fluctuating response (consisting of Kelvin and Poincaré waves) generated relative vorticity by the stretching and compression of planetary vortex lines as the waves propagate away from the adjustment region setting up boundary currents in their wake. This was followed by a much slower, nonlinear phase where advection of fluid columns rearranges the initial potential vorticity distribution. More recently, Stern & Helfrich (2002) investigated the temporal evolution of the boundary current, generated by the geostrophic adjustment process in a two-layer fluid, in order to model rotating boundary currents which are readily observable in the coastal ocean (Dorman 1987) and the atmospheric boundary layer (Gill 1982).

The energetics of linear geostrophic adjustment processes have also been studied extensively for both homogeneous (Gill 1982; Middleton 1987) and two-layer fluids (Ou 1986; van Heijst & Smeed 1986; Boss & Thompson 1995), with particular attention given to the partitioning of energy between the two components (geostrophic and fluctuating) of the response. Gill (1982) defined the available potential energy (APE) released by the adjustment process to be the difference between the potential energy associated with the initial unbalanced state and the potential energy residing in the final geostrophic component of the response. Gill (1982) concluded that for an infinite domain the kinetic energy of the geostrophic response accounted for one third of the APE while the remaining two thirds resided in the fluctuating response. Van Heijst & Smeed (1986) considered a baroclinic geostrophic adjustment in a semi-infinite domain and found that the partitioning of energy was a function of the distance between the front and a boundary which lies parallel to that front. Specifically, the kinetic energy of the geostrophic response was found to vary between zero when the front was at the boundary and Gill's infinite domain limit of one third of the APE when the front was infinitely far from the boundary.

Our interest in the present study is in the dynamics and energetics of the adjustment in a fully bounded domain which traps the fluctuating response so that an end state consisting purely of a geostrophic response will not be realized. We define geostrophic adjustment to be the transition from an initial unbalanced state to a response consisting of geostrophic and fluctuating components with a signature over the entire domain. In particular, we investigate the baroclinic geostrophic adjustment in a rotating circular basin (figure 1).

The time taken for the initial adjustment at the step height discontinuity and the generation of a fluctuating response influenced by rotation is the inertial period (e.g. Gill 1982).

$$T_I = \frac{2\pi}{f}, \quad (1.1)$$

where  $f$  is the inertial frequency.

The closed nature of the circular basin introduces a second timescale given by

$$t_2 = \frac{2\pi R_0}{c_0}, \quad (1.2)$$

where  $R_0$  is the basin radius and  $c_0$  is the baroclinic phase speed;  $t_2$  characterizes the time taken for the gravest-mode Kelvin wave to propagate around the basin, establishing a boundary current in its wake. Time  $t_2$  represents the time at which the geostrophic and fluctuating responses are found over the entire domain.

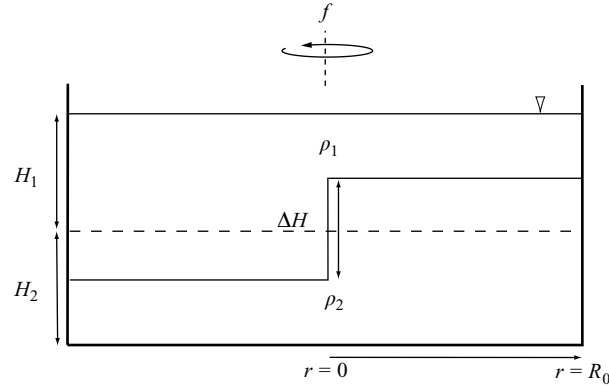


FIGURE 1. A side view of the initial condition for a baroclinic geostrophic adjustment in a circular basin of radius  $R_0$ . The step height discontinuity  $\Delta H$  across the tank diameter ensures that the upper ( $H_1$ ) and lower ( $H_2$ ) layer depths are equally displaced from the undisturbed position of the density interface.

Hermann *et al.* (1989) suggested that the timescale after which advective behaviour associated with the amplitude of an initial disturbance may be observed is given by

$$t_3 = \frac{2\pi H}{\Delta H f}, \quad (1.3)$$

where  $\Delta H$  is an initial step height discontinuity and  $H$  is the layer depth.

The model configuration given in figure 1 suggests that the geostrophic flow established in the bottom layer will be subject to Ekman damping, with a characteristic timescale for dissipation (e.g. Gill 1982) given by

$$t_4 = \frac{H_2}{\left(\frac{1}{2} f \nu\right)^{1/2}}, \quad (1.4)$$

after neglecting the interface deformation due to the initial condition.

The motivation for this study comes from recent work which focused on the large-scale hydrodynamic processes occurring within lakes for which the influence of Earth's rotation is important. Antenucci & Imberger (2001) used an analytical model to investigate the ratio of kinetic to potential energy for freely evolving basin-scale internal waves. The linear analysis of the basin-scale free motions in a circular basin discussed by Csanady (1967) and the analytical description of the linearized initial boundary value problem associated with the evolution of a surface tilt in a circular lake considered by Stocker & Imberger (2003) both indicate that the basin-scale response to an initial forcing consists of geostrophic and fluctuating components.

In this paper we describe a laboratory experiment to examine the response in a closed basin to an initial step function discontinuity in the internal density gradient. The experimental measurements are quantitatively compared with the corresponding solution of the linearized initial boundary value problem to determine the timescale over which such linearized solutions may be valid, given that both friction and nonlinear effects manifest themselves not only in the experiments described below but also in the field.

The remainder of the paper consists of the following. Section 2 introduces the experimental facility and the dimensionless parameters used to scale the problem. Laboratory experiments used to investigate the hydrodynamics of a baroclinic geostrophic

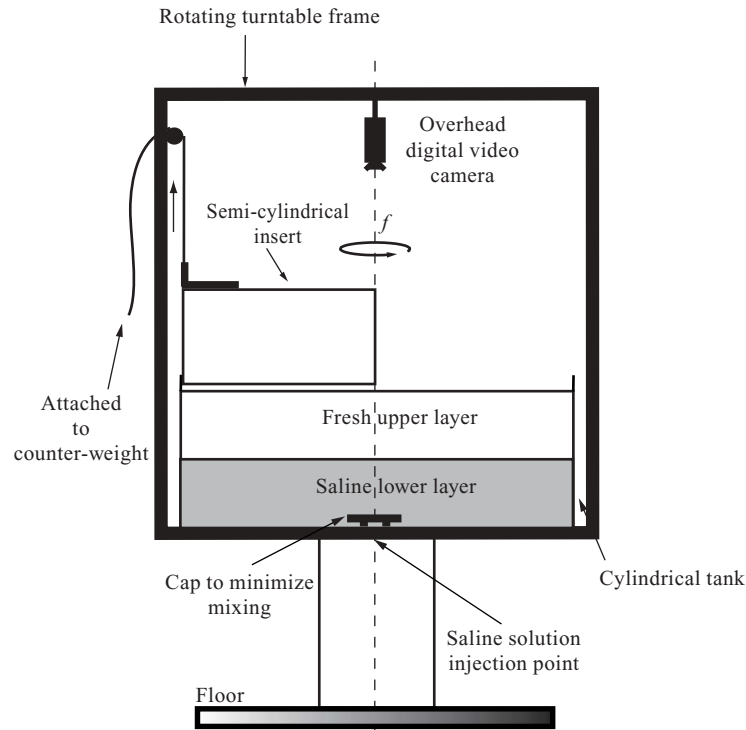


FIGURE 2. The rotating turntable facility.

adjustment in a circular basin are described in §3. In §4 we present an analytical solution for the steady component of the initial boundary value problem. In §5 we perform a quantitative comparison between the experimental and analytical approaches in order to determine the timescale over which linear solutions remain valid. In §6 we calculate the energetics for the linear geostrophic adjustment and the outcomes of this study are considered in terms of their application to lakes influenced by the rotation of the Earth.

## 2. Experimental facility

The model configuration and experimental setup are detailed in figures 1, 2 and 3. The experiments were conducted in a 95 cm diameter cylindrical Perspex tank of depth 50 cm. The tank was mounted on a rotating turntable that revolved counterclockwise at a constant rate  $f = 2\Omega$  (figure 2). The tank could be divided into two regions of equal volume by a removable semi-cylindrical Perspex insert (open at the top and bottom) that was raised or lowered by means of a pulley system attached to the rotating table-top frame (figure 2).

In a typical experiment, the tank was filled with fresh water to the desired upper-layer depth and allowed to spin up into solid body rotation. A saline solution was then carefully introduced beneath the lighter, fresher water until the desired lower-layer depth was achieved. The amount of mixing due to the insertion of the saline solution was minimized by placing a cap over the injection point that forced the introduced denser fluid out in a radial fashion. Once the fluid motions resulting from the filling process had dissipated and solid body rotation was re-established, the semi-cylindrical insert was carefully lowered into the tank to a depth of at least 5 cm below the

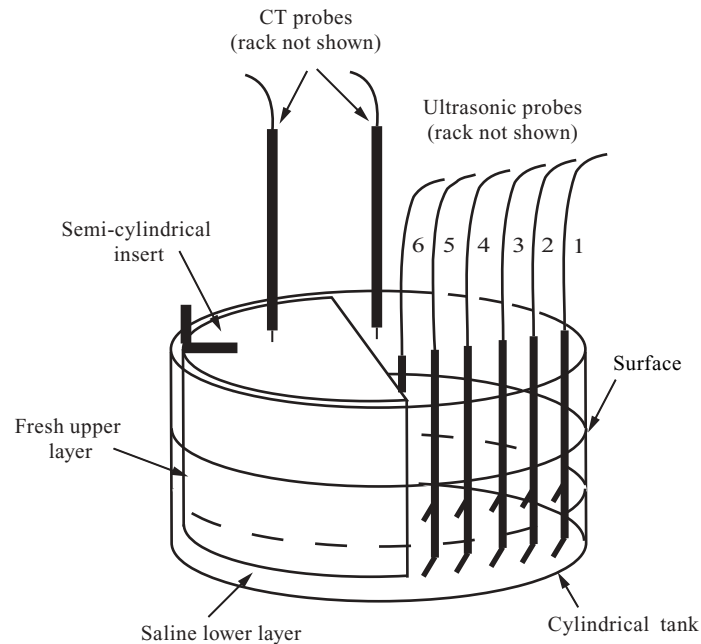


FIGURE 3. The experimental facility showing the position of the two conductivity-temperature (CT) probes and the radial distribution of the ultrasonic probes. The distances of the ultrasonic probes from the sidewall were 3 cm, 13 cm, 20 cm, 27 cm, 38 cm, and 45 cm respectively. The two-dimensional micro acoustic Doppler velocimeter (not shown) was placed adjacent to positions 1, 3 and 5 in subsequent repetitions of a given experimental run.

density interface, effectively partitioning the cylindrical tank into two regions: inside the semi-cylindrical insert (inner region) and outside the semi-cylindrical insert (outer region). A depression of the upper layer within the inner region was accomplished by pumping fluid from the upper layer in the outer region into the upper layer of the inner region which, in turn, drove a return flow of lower-layer fluid underneath the insert. Thickening of the density interface caused by pumping was minimized using a low pumping rate ( $8 \text{ ml s}^{-1}$ ) and by introducing the fresh water into the inner region via a horizontal diffuser.

This transfer pumping caused a stretching (in the upper layer of the inner region and the lower layer of the outer region) and compression (in the lower layer of the inner region and the upper layer of the outer region) of fluid columns, and as a consequence of the conservation of potential vorticity, introduced some relative vorticity into each layer of each region. As a result, the experiment was not initiated until this relative vorticity had dissipated (typically 2–3 hours). In this fashion, an initial potential energy and potential vorticity contrast between inner and outer regions was created.

Density profiles were taken in both the inner and outer regions, once the two-layer fluid had returned to its quiescent state, to measure the introduced step height discontinuity and to ensure that the density interface had not been thickened considerably during the setup process (figure 4). Profiles were obtained by traversing two conductivity-temperature (CT) probes (figure 3) over the total depth and then using the equations of Ruddick & Shirtcliffe (1979) to compute the fluid density. An experiment was initiated by swiftly removing the semi-cylindrical insert using the pulley system, while at the same time ensuring that the rotation rate remained constant.

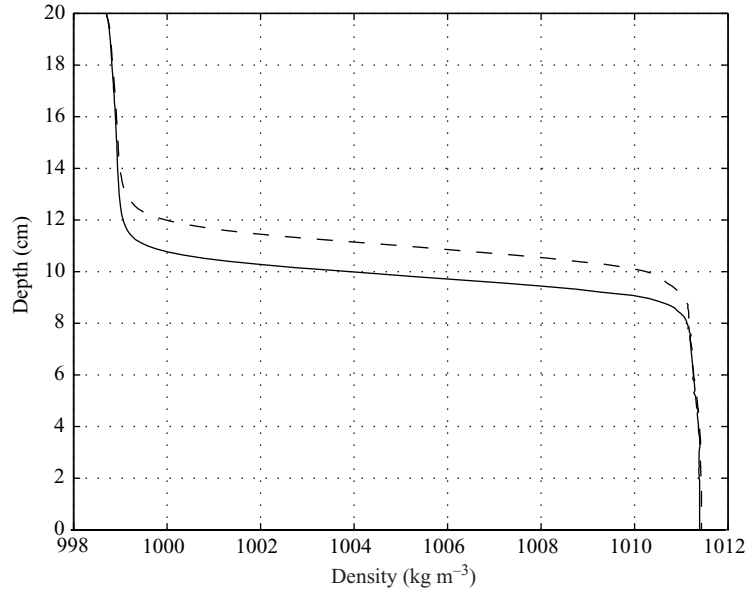


FIGURE 4. Density profiles taken from the CT probe located outside the semi-cylindrical insert before (solid line) and after (dashed line) the introduction of the potential energy step for run IV (see table 1).

Run	$\Delta H$	$H_1$	$H_2$	$g'$	$f$	$S$	$\epsilon$
I	1	10	10	6.3	0.44	0.25	0.1
II	2	10	10	18.8	0.19	1	0.2
III	2	10	10	17.1	0.25	0.75	0.2
IV	2	10	10	12.1	0.31	0.5	0.2
V	2	10	10	6.3	0.44	0.25	0.2
VI	4	10	10	18.8	0.19	1	0.4
VII	4	10	10	17.1	0.25	0.75	0.4
VIII	4	10	10	12.1	0.31	0.5	0.4
IX	8	10	10	18.8	0.19	1	0.8

TABLE 1. The experimental programme: all data in c.g.s. units.

The interface displacement created by the release was sampled at 5 Hz at six positions across the outer region by ultrasonic probes (figure 3) while the mid-depth upper-layer azimuthal and radial velocities were sampled at 10 Hz using a two-dimensional micro acoustic Doppler velocimeter (ADV). Each experimental run was repeated three times with the sample volume of the micro ADV being positioned adjacent to positions 1, 3 and 5 in each instance. Visualization experiments were also performed in which dye was injected at various locations in the upper layer and an overhead digital video camera mounted on the rotating turntable (figure 2) recorded the dye movement following the initiation of an experiment (figure 5).

A summary of the experimental programme is given in table 1. The interface profile  $\eta^*$  initially had a step height discontinuity across the tank diameter of magnitude  $\Delta H$  (figure 1). The upper and lower undisturbed layer depths were  $H_1$  and  $H_2$  respectively. The reduced gravity  $g'$  was varied between 6.3 and 18.8 cm s<sup>-2</sup> where  $g' = g\Delta\rho/\rho_2$  and  $\Delta\rho$  is the density difference between the upper and lower layers

$\rho_2 - \rho_1$  and  $g$  is the acceleration due to gravity. The radius of the semi-cylindrical forcing mechanism  $r_f$  was equal to the dimensional radius  $R_0$  of the cylindrical tank, as shown in figure 1, which was scaled with the baroclinic Rossby radius of deformation given by  $R = c_0/f$  where  $c_0 = (g'H_1H_2/(H_1 + H_2))^{1/2}$  is the linear baroclinic phase speed to give the Burger number  $S = c_0/R_0f$ , which provides a measure of the relative importance of stratification versus rotation (e.g. Antenucci & Imberger 2001). The inertial frequency  $f$  range was 0.19–0.44 s<sup>-1</sup> so that  $S$  varied between 1 and 0.25 and the interface displacement due to the centrifugal force is negligible (< 0.1 cm). The initial step discontinuity  $\Delta H$  was scaled by the undisturbed upper-layer depth  $H_1$  so that  $\epsilon = \Delta H/H_1$  was the dimensionless forcing amplitude while the interface displacement  $\eta^*$  was non-dimensionalized by  $\Delta H$  so that  $\eta = \eta^*/\Delta H$  was the dimensionless displacement of the density interface from its mean position. The scaled depth  $\epsilon$  was varied between 0.1 and 0.8, and the ratio of the layer depths  $H_1/H_2$  was unity. Time  $t$  was scaled using the inertial period  $T_I = 2\pi/f$  so that  $\tau = t/T_I$  was dimensionless time and the velocity was scaled using  $\epsilon f R$  so that the dimensionless azimuthal and radial velocities in the upper layer were  $\bar{u}_a$  and  $\bar{u}_r$  respectively.

### 3. Evolution of the geostrophic adjustment process in a rotating circular basin

The geometry of the problem indicates that the initial step height discontinuity introduced a symmetry between the upper and lower layers prior to the initiation of an experiment (figure 1). In the following, we describe in detail the hydrodynamics of the upper layer since the fundamental processes identified within this layer occur simultaneously in the lower layer, although velocities are in the opposite direction to their upper layer counterpart.

Results from a typical experimental run (run IV) are shown in figures 5, 6 and 7. Figure 5 details the results of a dye study while figures 6(a) and 7(a) present time series measurements of the interface displacement and azimuthal velocity, respectively. Consider first the plan view images taken from the dye study for run IV (figure 5). Regard each image as consisting of two semi-circular regions, the initially shallower upper layer in the upper half of the circular basin (shallow half) and the initially deeper upper layer in the lower half of the basin (deep half) (see figure 5(a)). Dye patches were inserted into the upper layer, four at the basin boundary (labelled A and B in the shallow half and C and D in the deep half) and one either side of the step discontinuity (labelled E in the shallow half and F in the deep half). The removal of the barrier dividing the two halves of the basin resulted in a horizontal pressure gradient initially driving a buoyant flow down gradient. The pressure gradient is quickly balanced by the Coriolis force and the resulting thermal wind balance induces a geostrophic mean flow which propagates parallel to the initial step across the width of the basin diameter. This geostrophic mean flow is captured by the movement of dye patches E and F between figures 5(a) and 5(c), but is most noticeable at later times by the movement of dye patches A and D between figures 5(e) and 5(f).

Concomitantly, Kelvin waves of elevation (located at point X in figure 5(a)) and depression (located at point Y in figure 5(a)) are generated at the sidewall boundaries of the basin. The wave of depression propagates cyclonically along the boundary into the shallow half of the basin, stretching planetary vorticity lines (Hermann *et al.* 1989). Such action induces positive relative vorticity which results in a cyclonic boundary current trailing the wave (Stern & Helfrich 2002). This is illustrated by the movement of dye patches A and B between figures 5(a) and 5(d). Similarly, the wave of elevation

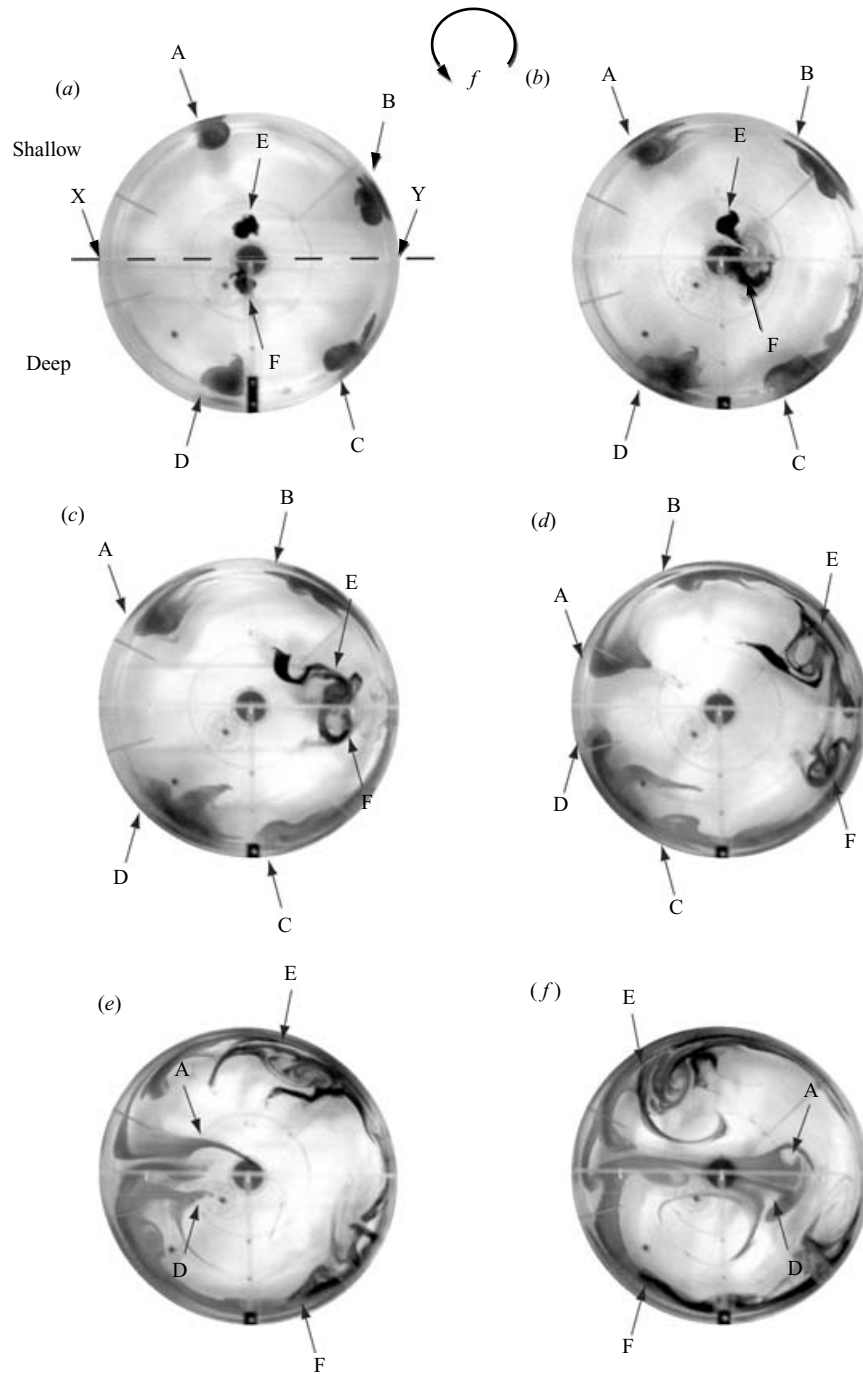


FIGURE 5. Plan view images of streak lines produced from dye inserted into the upper layer for run IV. Each image consists of two semi-circular regions, the initially shallower upper layer in the upper half of the circular basin (shallow half) and the initially deeper upper layer in the lower half of the basin (deep half). The dashed line in (a) indicates the position of the barrier which separates the shallow half and the deep half prior to its removal. The original positions of the dye patches before the initiation of the experiment are labelled A–F. Upon removal of the barrier, a Kelvin wave of depression is generated at Y and Kelvin wave of elevation at X. The location of the dye patches (b) after  $1T_l$ , (c) after  $3T_l$ , (d) after  $6T_l$ , (e) after  $10T_l$ , (f) and after  $15T_l$  are presented. Rotation is in a counter-clockwise direction.

propagates cyclonically along the boundary into the deep half, compressing planetary vorticity lines. This induces negative relative vorticity and generates an anticyclonic boundary current trailing the wave. This process is depicted by the movement of the dye patches C and D between figures 5(a) and 5(d).

The cyclonic flow in the initially shallow half and the anticyclonic flow in the initially deep half create regions of flow divergence (illustrated by the movement of dye patches E and F between figures 5(c) and 5(d)) and convergence (illustrated by the movement of dye patches A and D between figures 5(d) and 5(e)) located at the intersection of the initial step discontinuity with the sidewall boundaries of the basin. The connectivity between these two regions is provided by the geostrophic mean flow across the basin, resulting in a geostrophically balanced double gyre consisting of a cyclonic circulation in the shallow half (illustrated by the movement of dye patches A and E between figures 5(d) and 5(f)) and an anticyclonic circulation in the deep half (illustrated by the movement of dye patches D and F between figures 5(d) and 5(f)).

Now consider a typical example of the interface displacement and azimuthal velocity time series presented in figures 6(a) and 7(a) respectively. These illustrate that the fluctuating component of the response consisted of a range of frequencies. For all time series measurements, the fluctuating motion decayed in time with no significant wave motion evident after  $40T_I$ . A comparison of the time series collected from ultrasonic probes and from the micro ADV at positions 1 and 5 clearly shows that the amplitude of the fluctuating response decays offshore.

Power spectra for the interface displacement and velocity time series in figures 6(a) and 7(a) are shown in figures 6(b) and 7(b) respectively. When the dimensionless wave frequency  $\sigma = w/f < 1$  a wave is classified as a Kelvin (sub-inertial) wave and when  $\sigma > 1$  it is classified as a Poincaré (super-inertial) wave (Csanady 1967). Comparison of the interface displacement and velocity power spectra in figures 6(b) and 7(b) clearly indicates a sub-inertial peak and two super-inertial peaks at almost identical frequencies which suggests that the fluctuating response for run IV consists of a Kelvin and two Poincaré modes.

The frequencies identified from the interface displacement and velocity power spectra in figures 6(b) and 7(b) are compared with the predictions of wave frequency for linear basin-scale baroclinic waves so that the modal structure (azimuthal, radial) and direction of propagation (cyclonic (–) or anticyclonic (+)) may be determined. For Poincaré waves the dispersion relation is given by

$$\frac{1}{S} \sqrt{(\sigma)^2 - 1} J_{n-1} \left( \frac{1}{S} \sqrt{(\sigma)^2 - 1} \right) + n \left( \frac{1}{\sigma} - 1 \right) J_n \left( \frac{1}{S} \sqrt{(\sigma)^2 - 1} \right) = 0 \quad (3.1)$$

where  $J_n$  is the Bessel function of real argument of order  $n$ , where  $n$  is the azimuthal mode number. Equation (3.1) is an eigenvalue problem for which solutions of increasing  $\sigma$  correspond to higher radial modes for fixed  $n$  (e.g. Antenucci & Imberger 2001). A frequency equation of identical form to (3.1) is obtained for Kelvin waves using the identity  $J_n(ix) = i^n I_n(x)$  after noting that the coefficient of the first term and the argument of the Bessel function in (3.1) is imaginary for a Kelvin wave (Csanady 1967). For run VI the fluctuating response consists of a cyclonic (1,1) Kelvin wave, an anticyclonic (1,1) Poincaré wave and a cyclonic (2,1) Poincaré wave.

A summary of the waves excited for each run is given in table 2. It is evident that the wave field exhibits a functional dependence on  $S$ , with higher azimuthal modes being excited as the influence of rotation becomes more important (table 2).

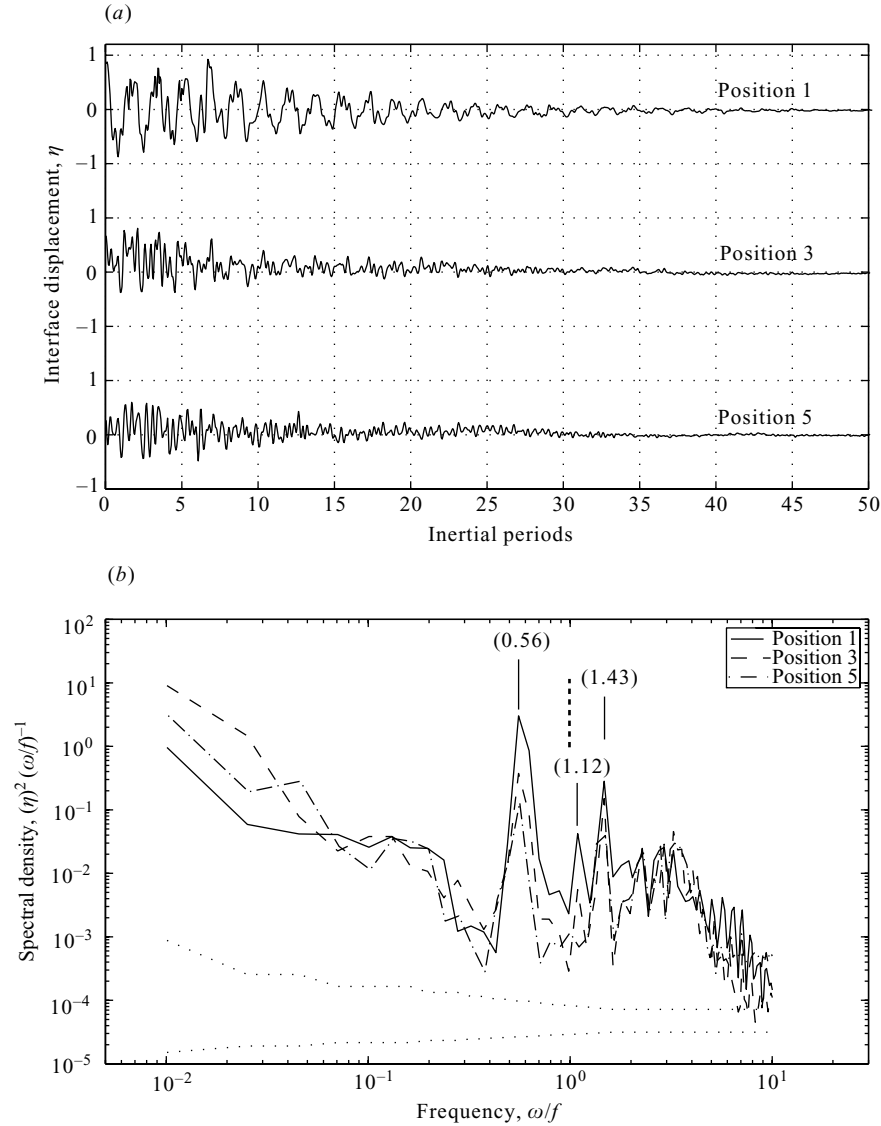


FIGURE 6. (a) Time series of the interface displacement  $\eta$  collected at 5 Hz by the ultrasonic probes from positions 1, 3 and 5 for run IV. (b) Power spectra of the interface displacements shown in (a), with positions 1, 3 and 5 being represented by the solid, dashed and dash-dot lines respectively. The wave frequency  $\omega$  is scaled by  $f$ . The dashed vertical line identifies the inertial frequency  $f$  while the solid vertical lines identify the significant peaks which consist of a sub-inertial wave and two super-inertial waves. Spectra have been smoothed in the frequency domain to improve confidence, with the 95% confidence level given as the difference between the two dotted lines at a prescribed frequency (e.g. Bendat & Piersol 2000).

Lamb (1932) used linear inviscid theory to argue that for a Kelvin wave solution of azimuthal mode  $n$  to exist, it must satisfy

$$S < \left[ \frac{1}{n(n+1)} \right]^{1/2}. \quad (3.2)$$

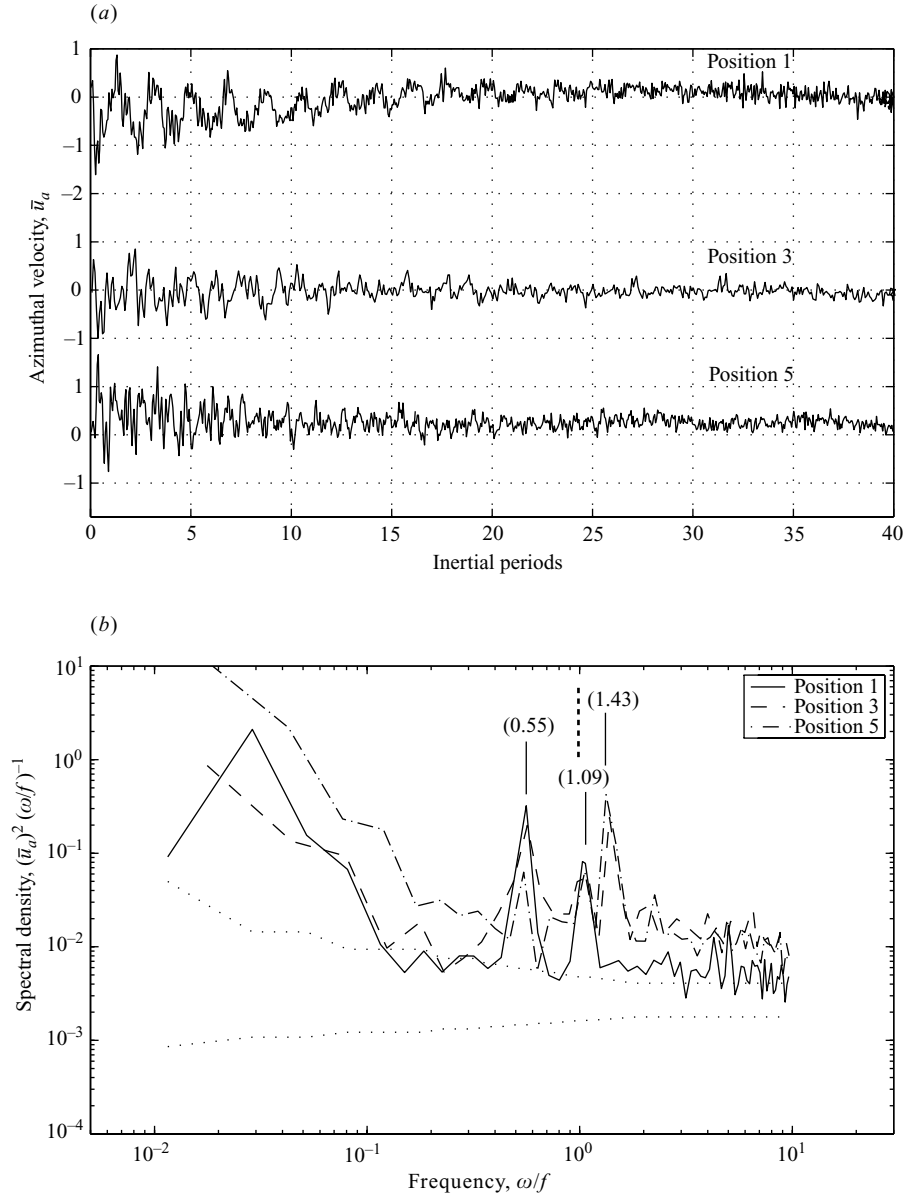


FIGURE 7. (a) Time series of the azimuthal velocity  $\bar{u}_a$  collected at 10Hz by the two-dimensional micro ADV from positions 1, 3 and 5 for run IV. (b) Power spectra of the azimuthal velocity shown in (a), with positions 1, 3 and 5 being represented by the solid, dashed and dash-dot lines respectively. The wave frequency  $\omega$  is scaled by  $f$ . The dashed vertical line identifies the inertial frequency  $f$  while the solid vertical lines identify the significant peaks which consist of a sub-inertial wave and two super-inertial waves. Spectra were smoothed in a similar manner to figure 6.

This criterion accurately predicts the number of Kelvin waves excited for all laboratory experiments except when  $S = 0.75$ . Inspection of (3.2) indicates that when  $S > 1/\sqrt{2}$  no Kelvin wave can exist, contradicting the experimental observation that a Kelvin wave is excited when  $S = 0.75 > 1/\sqrt{2}$  (see table 2). While (3.2) is derived from linear inviscid theory, the waves generated in the laboratory experiment are influenced by

---

$S$	Mode	Frequency	Type
1	$-(1, 1)$	Super-inertial	Poincaré wave
	$+(1, 1)$	Super-inertial	Poincaré wave
0.75	$-(1, 1)$	Sub-inertial	Kelvin wave
	$+(1, 1)$	Super-inertial	Poincaré wave
0.5	$-(1, 1)$	Sub-inertial	Kelvin wave
	$-(2, 1)$	Super-inertial	Kelvin wave
	$+(1, 1)$	Super-inertial	Poincaré wave
0.25	$-(1, 1)$	Sub-inertial	Kelvin wave
	$-(2, 1)$	Sub-inertial	Kelvin wave
	$-(3, 1)$	Sub-inertial	Kelvin wave
	$+(1, 1)$	Super-inertial	Poincaré wave

---

TABLE 2. The dominant basin-scale baroclinic waves observed in the laboratory experiments. The direction of propagation ( $(-)$  cyclonic or  $(+)$  anticyclonic) and modal structure (given above as (azimuthal mode, radial mode)) are assigned on the basis of a comparison of the measured frequencies with the theoretical predictions of wave frequency (3.1). The excited modes are independent of the initial forcing,  $\epsilon$ .

---

friction. Frictional effects lead to a reduction in the phase speed which, in turn, leads to the observed reduction in wave frequency (Martinsen & Weber 1981). In this instance, we suggest that the effect is sufficient to shift the predicted super-inertial wave into the sub-inertial range (see table 2).

In summary, the analysis of dye visualization experiments and of the interface displacement and velocity time series, clearly illustrate the temporal evolution of the geostrophic adjustment process in a rotating circular basin, from an initially unbalanced state to a response consisting of geostrophic and fluctuating components.

#### 4. Steady solution of the initial boundary value problem

Consider the initial state of the two-layer fluid contained in the cylindrical tank as presented in figure 1. The initial dimensional interface profile  $\eta^*$  has a discontinuity in its height across the tank diameter of magnitude  $\Delta H$ . It is assumed that both  $\Delta H/H_1 \ll 1$  and  $\Delta H/H_2 \ll 1$ , so that the starting point of the analysis is the rotating shallow water equations (Gill 1976).

These are made dimensionless, using the inertial period  $T_I$  as the timescale, the baroclinic radius of deformation  $R$  as the horizontal lengthscale and  $\epsilon f R$  as the velocity scale in each layer, where  $\epsilon = \Delta H/H_1$ . The ratio of the depths  $\delta = H_1/H_2$  is assumed to be order one.

The dimensionless equations for the upper layer (layer 1) are

$$\frac{1}{2\pi} \mathbf{u}_{1\tau} + \epsilon \mathbf{u}_1 \cdot \nabla \mathbf{u}_1 + \mathbf{k} \times \mathbf{u}_1 = -\nabla p_1, \quad (4.1a)$$

$$-\frac{1}{2\pi} \eta_\tau + \nabla \cdot [\mathbf{u}_1(1 - \epsilon\eta)] = 0, \quad (4.1b)$$

and for the lower layer (layer 2) they are

$$\frac{1}{2\pi} \mathbf{u}_{2\tau} + \epsilon \mathbf{u}_2 \cdot \nabla \mathbf{u}_2 + \mathbf{k} \times \mathbf{u}_2 = -\nabla p_2, \quad (4.2a)$$

$$\frac{1}{2\pi} \delta \eta_\tau + \nabla \cdot [\mathbf{u}_2(1 + \delta\epsilon\eta)] = 0, \quad (4.2b)$$

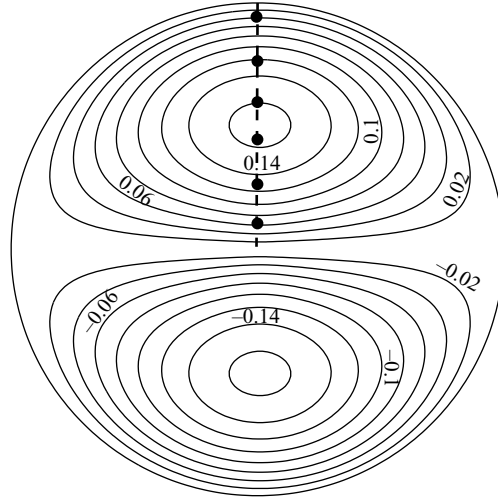


FIGURE 8. Contour plot of the interface displacement  $\eta$  for the geostrophically balanced double gyre for  $S=0.5$ , calculated from (4.3) using a contour interval of 0.02. The dashed line is the radial transect along which the ultrasonic probes, indicated by the dots, were positioned in the laboratory experiment (figure 3).

where  $\mathbf{u}_n$  and  $p_n$  are the velocities and pressures in the  $n$ th layer respectively and  $\eta = \eta^* / \Delta H$  is the dimensionless displacement of the density interface from its mean position. The relationship between the pressures is  $p_2 = p_1 + (1 + \delta)\eta$ . For convenience, the dimensionless radius of the circular basin is  $R_0/R = r_f/R = S^{-1}$  and the free surface is assumed to be fixed.

The derivation of the steady, geostrophically adjusted linear solution to (4.1) and (4.2), subject to the initial and boundary conditions, is provided in Appendix A. The steady solution to the initial boundary value problem is

$$\eta = -\frac{2}{\pi} \sum_{n=0}^{\infty} \frac{1}{2n+1} f_{2n+1}(r) \sin(2n+1)\theta, \quad (4.3)$$

where

$$f_n(r) = \frac{K_n(S^{-1})I_n(r)}{I_n(S^{-1})} \int_0^{S^{-1}} \xi I_n(\xi) d\xi - I_n(r) \int_r^{S^{-1}} \xi K_n(\xi) d\xi - K_n(r) \int_0^r \xi I_n(\xi) d\xi. \quad (4.4)$$

Equation (4.3) represents a geostrophically balanced double gyre (figure 8) which satisfies  $\nabla^2 \eta - \eta = -(1/2) \text{sgn} \theta$ .

## 5. Quantitative comparison of the laboratory experiments and the analytical solution

If we non-dimensionalize the timescales (1.2), (1.3) and (1.4) by the inertial period  $T_I$  then

$$\tau_2 = \frac{R_0}{R} = S^{-1}, \quad (5.1)$$

$$\tau_3 = \frac{H_1}{\Delta H} = \epsilon^{-1}, \quad (5.2)$$

$$\tau_4 = \frac{H_2}{\pi} \left( \frac{f}{2\nu} \right)^{1/2} = \tau_D. \quad (5.3)$$

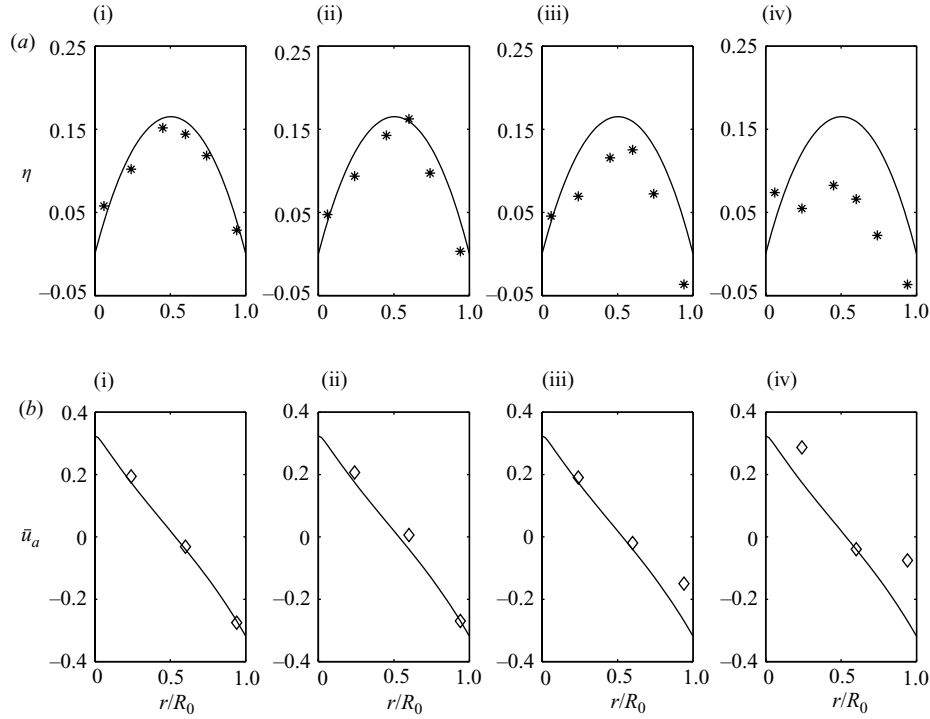


FIGURE 9. Comparison between the experimental and analytical profiles of the geostrophic component along the radial transect, indicated in figure 3, for run IV ( $S=0.5$ ,  $\epsilon=0.2$ ) after (i)  $3T_I$ , (ii)  $6T_I$ , (iii)  $10T_I$ , (iv)  $15T_I$ , (a) for the interface displacement  $\eta$ , (b) for the azimuthal velocity  $\bar{u}_a$ . The solid line is the analytical solution while the asterisks and diamonds are the measured interface displacements and azimuthal velocities respectively. Error estimates calculated from the variance between repetitions of an experimental run were of the order of instrument sensitivity ( $\pm 0.02$  for the ultrasonic probes and  $\pm 0.04$  for the micro ADV).

The geostrophic and fluctuating components of the response were separated by low-pass filtering the interface displacement and velocity time series. The cut-off frequency of the low-pass filter was chosen as the frequency of the gravest fluctuating mode. Noting (1.2) and (5.1), the low-pass-filtered signal was applicable for non-dimensional times greater than  $S^{-1}$  and provided point measurements of the temporal evolution of the geostrophic interface displacement and velocity along the radial transect shown in figure 3.

This procedure was used to compare the measured radial interface displacement and velocity profiles with the prediction of the analytical solution (4.3) for the geostrophic response. The results for run IV are shown in figure 9. The observed interface displacement and velocity profiles and their analytical predictions coincide after  $3T_I$  (see panel (i) of figures 9(a) and 9(b)) and still exhibit excellent agreement after  $6T_I$  (see panel (ii) of figures 9(a) and 9(b)). After  $10T_I$  the interface displacement observations begin to deviate from the predictions (see panel (iii) of figure 9(a)) while after  $15T_I$  the agreement deteriorates for both the interface displacement and velocity measurements (see panel (iv) of figures 9(a) and 9(b)). Similar results were obtained in experiments where the initial forcing was the same as for run IV but  $S$  (the influence of rotation) was varied. In run V for example, both the observed interface displacement and velocity profiles are in excellent agreement with the analytical

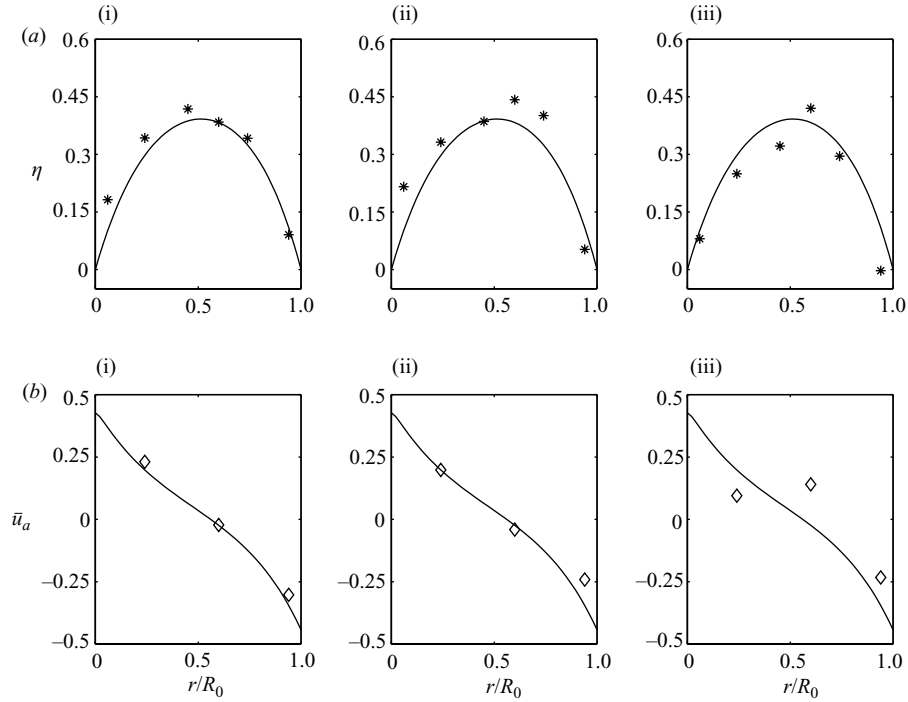


FIGURE 10. Comparison between the experimental and analytical radial profiles of the geostrophic component for run V ( $S = 0.25$ ,  $\epsilon = 0.2$ ) after (i)  $6T_I$ , (ii)  $10T_I$ , (iii)  $15T_I$ , (a) for the interface displacement  $\eta$ , (b) for the azimuthal velocity  $\bar{u}_a$ . The solid line is the analytical solution while the asterisks and diamonds are the measured interface displacements and azimuthal velocities respectively. Error estimates were identical to those calculated in figure 9.

predictions after  $6T_I$  (see panel (i) of figures 10(a) and 10(b)), but after  $10T_I$  both the interface displacement and velocity profiles exhibit slight deviations from the analytical solution (see panel (ii) of figures 10(a) and 10(b)). The deviations become pronounced after  $15T_I$ , and are particularly apparent in the velocity observations (see panel (iii) of figure 10(a)).

In figure 11 we show results for run VIII, which was conducted at the same  $S$  as run IV but with twice the initial forcing  $\epsilon$ . The observations of both the interface displacement and velocity are in excellent agreement with the predictions after  $3T_I$  (compare panel (i) in figures 9 and 11). This agreement, however, deteriorates noticeably after  $6T_I$  for both the interface displacement and velocity observations (compare panel (ii) in figures 9 and 11) and becomes more pronounced for longer time (see panels (iii) and (vi) in figure 11). In summary, the results in figures 9–11 suggest that as the value of  $\epsilon = \Delta H/H_1$  increases, the predictions of linear theory increasingly overestimate the observed response, particularly in the displacement field.

In figure 12 the experimental results are summarized with  $\epsilon^{-1}$  defined in (5.2) plotted against time. The dimensionless timescale for the establishment of the double gyre ( $S^{-1}$ ) as well as the dimensionless dissipation timescale ( $\tau_D$ ) are also included in figure 12. Experimental observations indicate that the geostrophic double gyre is present after approximately  $S^{-1}$ , although owing to the limitation of the filtering technique used to obtain this result, this represents an upper bound for the transition

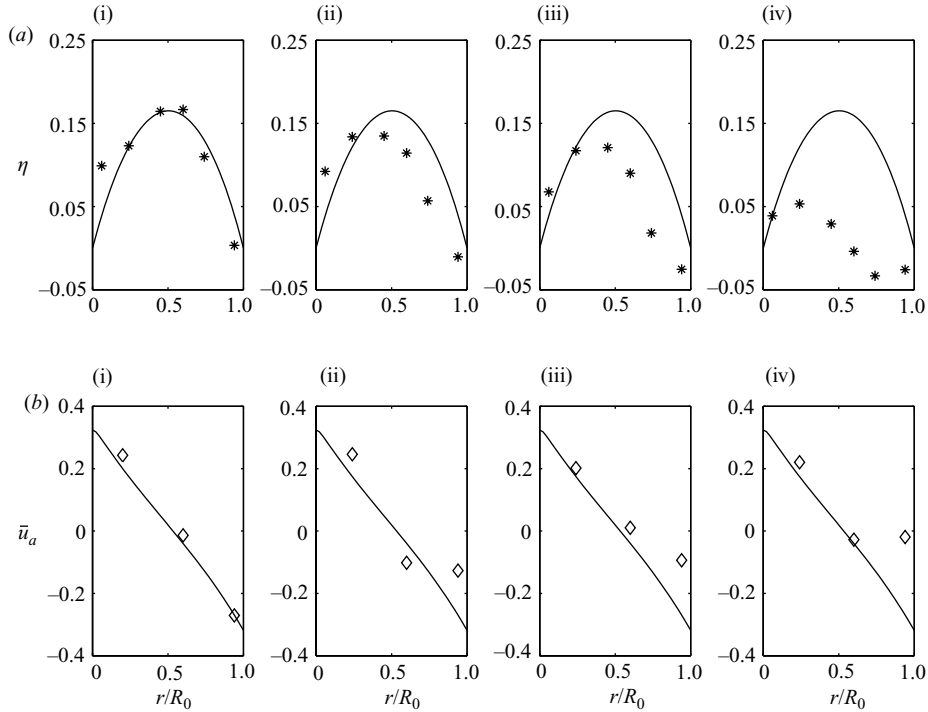


FIGURE 11. Comparison between the experimental and analytical radial profiles of the geostrophic component for run VIII ( $S=0.5$ ,  $\epsilon=0.4$ ) after (i)  $3T_I$ , (ii)  $6T_I$ , (iii)  $10T_I$ , (iv)  $15T_I$ , (a) for the interface displacement  $\eta$ , (b) for the azimuthal velocity  $\bar{u}_a$ . The solid line is the analytical solution while the asterisks and diamonds are the measured interface displacements and azimuthal velocities respectively. Error estimates were of the order of instrument sensitivity ( $\pm 0.01$  for the ultrasonic probes and  $\pm 0.02$  for the micro ADV).

from the initial condition (see figure 12). The time after which experimental observations depart from linear, inviscid theory is also shown in figure 12. This dividing line is linearly proportional to  $\epsilon^{-1}$  over the experimental programme with a slope of approximately  $1/2$ . The  $\tau_D$  curve intersects this line for large  $\epsilon^{-1}$ , suggesting that when  $2\epsilon^{-1} < \tau_D$  the primary mechanism responsible for the observed departure is the nonlinear advection of fluid columns, and when  $2\epsilon^{-1} > \tau_D$  frictional dissipation is the likely mechanism.

Using the timescales determined from figure 12, a strong forcing is defined as  $2\epsilon^{-1} < S^{-1}$  and  $2\epsilon^{-1} < \tau_D$ , a moderate forcing as  $S^{-1} < 2\epsilon^{-1} < \tau_D$ , and a weak forcing as  $S^{-1} < \tau_D < 2\epsilon^{-1}$ . Note that for a strong forcing  $\epsilon = O(1)$ , which is beyond the validity of the linear solution presented in §4, so that only moderate and weak forcings are considered during the experimental programme (see table 1).

In this way, four regimes can be identified in figure 12: a linear adjustment regime, which can be sub-divided into two phases (see below), and two further regimes in which either advective or dissipative effects dominate.

The linear adjustment regime is separated into a transition phase from the initial condition to the geostrophically balanced double gyre ( $1 < \tau < S^{-1}$ ), and a subsequent continuation phase where the double gyre is sustained until advective ( $S^{-1} < \tau < 2\epsilon^{-1}$ , moderate forcing) or dissipative ( $S^{-1} < \tau < \tau_D$ , weak forcing) effects become important.

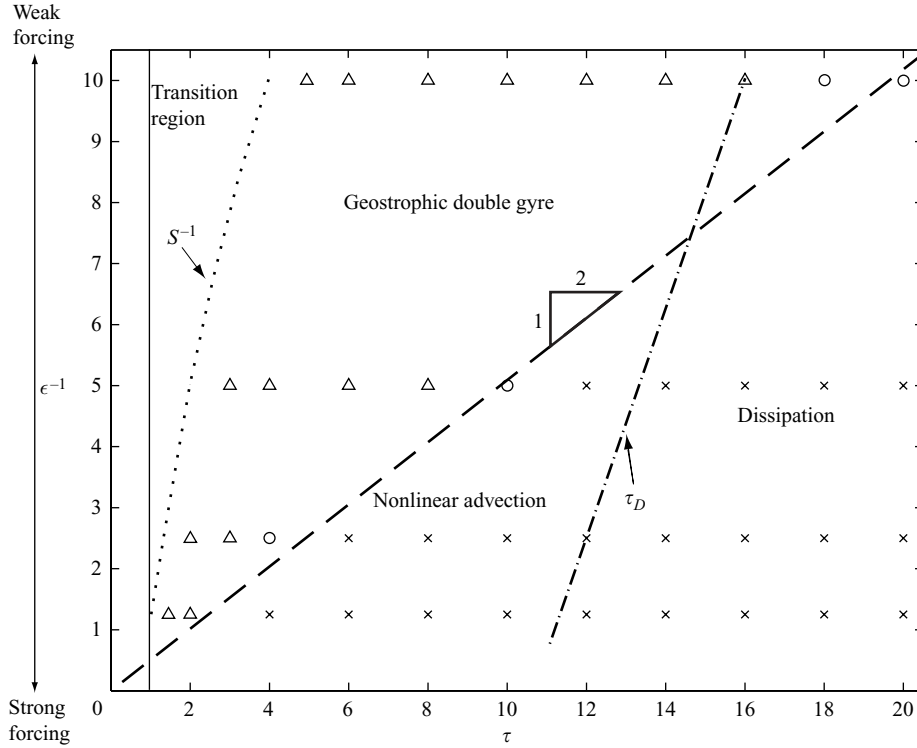


FIGURE 12. The dimensionless nonlinear timescale  $\epsilon^{-1}$  versus the temporal evolution of geostrophic double gyre observed in the experimental programme. The measured radial profiles of interface displacement and velocity are qualitatively compared with the analytical solution. A strong agreement for both interface displacement and velocity is represented by a triangle, a strong agreement for one of the measured quantities is represented by a circle, while a weak agreement for both is represented by a cross. The dotted line separates the linear phase into two distinct regions and indicates the time after which the geostrophically balanced double gyre is observed. The dashed line through the origin, which has a slope of approximately  $1/2$ , indicates the time after which observations depart from linear, inviscid theory, while the dash-dot line indicates the dissipation timescale  $\tau_D$ . The solid vertical line at  $\tau = 1$  is the dimensionless inertial period. Data from run I ( $S = 0.25$ ,  $\epsilon = 0.1$ ), run IV ( $S = 0.5$ ,  $\epsilon = 0.2$ ), run VII ( $S = 0.75$ ,  $\epsilon = 0.4$ ), and run IX ( $S = 1$ ,  $\epsilon = 0.8$ ) of the experimental programme have been used.

## 6. Discussion

The excellent agreement between (4.3) and the laboratory experiments during the linear phase allows us to use the analytical solution with confidence to examine the distribution of initial potential energy  $IPE$  (the energy in the initial unbalanced state) between the geostrophic and fluctuating components during this period. Expressions for the kinetic  $KE$ , potential  $PE$ , and total energy  $TGE$  residing in the geostrophic component are derived from the analytical solution (see Appendix A for the details) and are plotted in figure 13 as a function of the Burger number  $S$ . It is evident from this plot that the distribution of  $IPE$  between geostrophic energy  $TGE$  and wave energy  $TWE$  (where  $TWE = IPE - TGE$ ) is dependent upon  $S$ . Similarly, the available potential energy  $APE$  (where  $APE = IPE - PE$ ) exhibits a functional dependence on  $S$  with the ratio of geostrophic kinetic energy to available potential energy

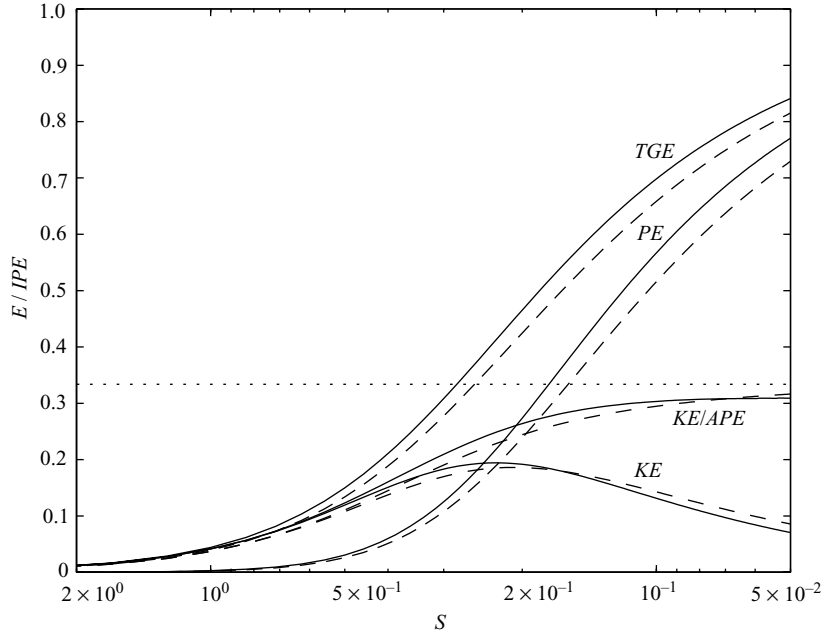


FIGURE 13. The energetics of the geostrophic component, as a function of  $S = R/r_f$ , calculated from (4.3) for an initial step height discontinuity (solid lines) and for an initial linear tilt of the density interface (dashed lines) (Stocker & Imberger 2003). For a given value of  $S$ , the energy in the geostrophic component ( $TGE$ ) is given by the sum of the kinetic ( $KE$ ) and potential ( $PE$ ) energy while the wave energy  $TWE$  is the difference between the initial potential energy  $IPE$  and  $TGE$ . The ratio of geostrophic kinetic energy to available potential energy ( $APE$ ) asymptotically approaches the infinite domain limit of  $1/3$  (the horizontal dotted line) (Gill 1982) as  $S \rightarrow 0$ . All quantities have been normalized by the initial potential energy.

asymptotically approaching the infinite domain limit of  $1/3$  noted by Gill (1982) as  $S \rightarrow 0$ . Comparison of the energetics calculated from the solution to the initial linear interface tilt problem provided by Stocker & Imberger (2003) and (4.3) reveals that the kinetic, potential, and total geostrophic energy, as well as the ratio of geostrophic kinetic energy to available potential energy, exhibit a similar functional dependence on  $S$  (see figure 13). The suggestion is that irrespective of the exact nature of the basin-scale initial forcing, the response is characterized by a geostrophic double gyre plus a fluctuating component with similar partitioning of energy among the components.

In the field an external disturbance such as a basin-scale surface wind stress typically provides the forcing (e.g. Saggio & Imberger 1998; Antenucci & Imberger 2001). For lakes influenced by the Earth's rotation, the response to a unidirectional, basin-scale external wind forcing has been modelled numerically (Serruya, Hollan & Bitsch 1984) and analytically (Stocker & Imberger 2003) and shown to consist of a geostrophic double gyre and baroclinic basin-scale waves. Lake Kinneret (Israel) is subject to a basin-scale wind forcing, and Herman (1989) noted that Landsat images of a peridinium bloom bear a remarkable resemblance to the double gyre configuration, while Antenucci & Imberger (2001) observed that the internal wave field was dominated by Kelvin and Poincaré waves. The results of the laboratory experiment are consistent with these field observations and are representative of the response to a basin-scale wind forcing for large lakes influenced by the Earth's rotation.

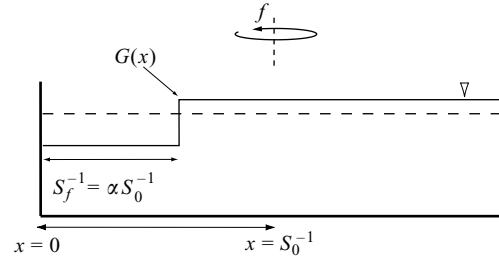


FIGURE 14. The one-dimensional problem where the initial profile  $G(x)$  has a step height discontinuity located at  $S_f^{-1} = r_f/R_0$  which is expressed as a function of  $S_0^{-1} = R_0/R$ .

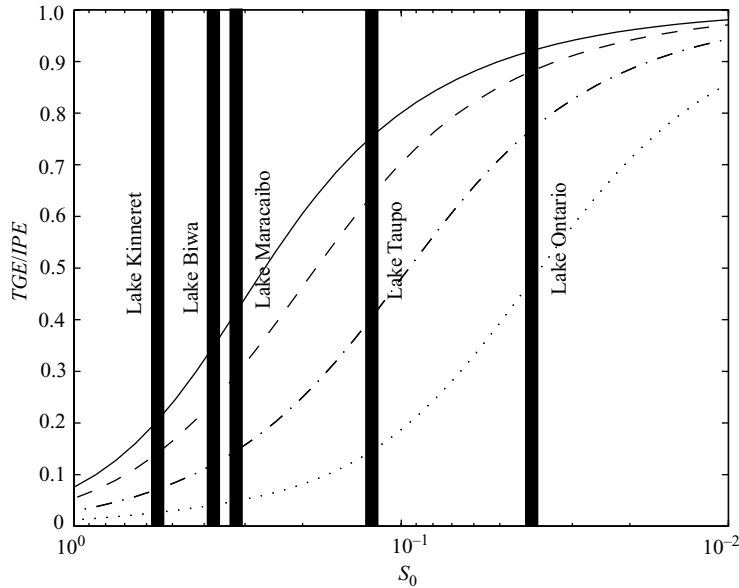


FIGURE 15. The energy in the geostrophic component ( $TGE$ ) as a function of  $S_0 = \alpha S_f$  for an initial step height discontinuity (see figure 14) where  $\alpha = 1$  (solid line),  $\alpha = 0.5$  (dashed line),  $\alpha = 0.25$  (dash-dot line), and  $\alpha = 0.1$  (dotted line). The vertical lines indicate the typical value of  $S_0$  for Lake Kinneret (Israel), Lake Maracaibo (Venezuela), Lake Biwa (Japan), Lake Taupo (New Zealand) and Lake Ontario (Canada) during the summer period (data taken from Antenucci & Imberger (2001)). All quantities have been normalized by the initial potential energy ( $IPE$ ).

When the forcing scale  $r_f$  is less than the basin scale  $R_0$ , however, the geostrophic response will not consist of a symmetric double gyre. Scaling  $r_f$  and  $R_0$  with  $R$  gives two Burger numbers: a Burger number based upon the scale of motion initially introduced by the forcing, given by  $S_f = R/r_f$ , and a Burger number associated with the basin-scale motions present once the linear geostrophic evolution process is complete, given by  $S_0 = R/R_0$ . Consider for example the one-dimensional problem presented in figure 14, which is a finite domain analogue of the semi-infinite domain study of van Heijst & Smeed (1986), where  $\alpha = r_f/R_0 = S_0/S_f$ . The energetics of the geostrophic component for various values of  $\alpha$  are presented in figure 15 and the details of these calculations can be found in Appendix B. For the lower ( $S_0 \rightarrow 0$ ) and upper ( $S_0 \rightarrow \infty$ ) limits, varying  $\alpha$  does not change the energy in the geostrophic

component. For intermediate values of  $S_0$  the dependence on  $\alpha$  and, hence, on the forcing scale  $r_f$  is significant. A number of lakes influenced by the rotation of the Earth have a value of  $S_0$  within this range during the summer months (see figure 15). Therefore, to obtain an accurate prediction of their response to wind-forcing, it is important to know the characteristic horizontal lengthscale of the wind event.

Antenucci & Imberger (2001) determined that the Burger number  $S_0$  is a critical parameter in the understanding of the partitioning of energy between potential and kinetic forms of the fluctuating response. The importance of each Burger number is now clear:  $S_f$  determines the partitioning of energy between the geostrophic and fluctuating components of the response, while  $S_0$  determines the partitioning of wave energy within the excited modes (Kelvin and Poincaré waves) of the fluctuating response.

We conclude by noting that the laboratory experiments clearly illustrate that analytical solutions are limited in their applicability when it comes to providing an accurate description of the longer term dynamics and energetics of lakes influenced by the rotation of the Earth. The long-time evolution of the geostrophic and fluctuating components subject to nonlinear and dissipative effects will therefore be addressed in subsequent studies.

The authors are grateful to Jason Antenucci, Andres Gomez and two anonymous referees for useful comments on initial drafts of this manuscript. G.W. acknowledges the support of an Australian Postgraduate Award and a Jean Rogerson Supplementary scholarship. R.M. is grateful for the Gleddon Visiting Senior Fellowship which enabled his visit to the Centre for Water Research.

This research was funded by the Australian Research Council and forms Centre for Water Research reference ED1649-GW.

### Appendix A. Linear baroclinic geostrophic adjustment in a circular domain

Defining the baroclinic velocity as  $\mathbf{u} = \mathbf{u}_1 - \mathbf{u}_2$  and neglecting terms of order  $\epsilon$  in (4.1) and (4.2) (Csanady 1967), it follows that

$$\frac{1}{2\pi} \mathbf{u}_\tau - \mathbf{k} \times \mathbf{u} = (1 + \delta) \nabla \eta, \quad (\text{A } 1a)$$

$$-\frac{1}{2\pi} (1 + \delta) \eta_\tau + \nabla \cdot \mathbf{u} = 0, \quad (\text{A } 1b)$$

in the absence of any external forcing. A single equation for  $\eta$  can be derived from (A 1) (Gill 1976), namely

$$\nabla^2 \eta - \frac{1}{4\pi^2} \eta_{\tau\tau} - \eta = -\eta_0 H(\tau), \quad r \leq S^{-1}, \quad (\text{A } 2)$$

where  $H(\tau)$  is the Heaviside function and

$$\eta_0 = -\frac{1}{2} \text{sgn } \theta, \quad -\pi < \theta \leq \pi, \quad (\text{A } 3)$$

is the initial displacement of the interface which, owing to the cylindrical geometry of the tank, is best written in terms of polar coordinates, where  $r$  is the radial and  $\theta$  the angular coordinate.

Here only the steady, geostrophically adjusted solution to (A 2) is sought. Accordingly

$$\nabla^2 \eta - \eta = -\eta_0, \quad (\text{A } 4)$$

which is equivalent to the conservation of quasi-geostrophic potential vorticity, is solved subject to the no-normal-flow boundary condition at the perimeter of the tank, i.e.  $\eta(S^{-1})=0$ . The solution of (A 4) is found by first writing  $\eta(r, \theta)$  as a complex Fourier series, i.e.

$$\eta = \sum_{n=-\infty}^{n=\infty} R_n(r) e^{in\theta}. \quad (\text{A } 5)$$

Note that

$$\eta_0 = -\frac{1}{2} \operatorname{sgn} \theta = \sum_{n=-\infty}^{\infty} c_n e^{in\theta}, \quad (\text{A } 6)$$

where

$$\begin{aligned} c_n &= \frac{1}{2\pi} \int_{-\pi}^{\pi} \left(-\frac{1}{2} \operatorname{sgn} \theta\right) e^{-in\theta} d\theta, \\ &= \begin{cases} i/(\pi n), & n \text{ odd,} \\ 0, & n \text{ even.} \end{cases} \end{aligned} \quad (\text{A } 7)$$

Hence, substituting (A 5) and (A 6) into (A 4), the radial modes  $R_n(r)$  satisfy

$$\frac{d}{dr} \left( r \frac{dR_n}{dr} \right) - \left( 1 + \frac{n^2}{r^2} \right) r R_n = r c_n, \quad (\text{A } 8)$$

and are such that  $R_n(S^{-1})=0$  and bounded at  $r=0$ . Equation (A 8) is in Sturm–Liouville form and its solution can be expressed as

$$R_n(r) = c_n \int_0^{S^{-1}} \xi g_n(r, \xi) d\xi, \quad (\text{A } 9)$$

where  $g_n(r, \xi)$  is the Green's function for (A 8) which can be constructed according to standard techniques (Boyce & DiPrima 1992). In particular,

$$g_n(r, \xi) = \frac{I_n(\xi) K_n(S^{-1}) I_n(r)}{I_n(S^{-1})} - \begin{cases} K_n(\xi) I_n(r), & r < \xi \\ I_n(\xi) K_n(r), & r > \xi, \end{cases} \quad (\text{A } 10)$$

where  $I_n$  and  $K_n$  are modified Bessel functions of order  $n$ . Substitution of (A 10) into (A 9) and using the fact that  $g_n = g_{-n}$  finally gives the steady geostrophically adjusted solution (4.3).

#### A.1. Linear energetics

Begin by considering a one-and-a-half-layer fluid. Working with the dimensionless quantities defined previously, the potential energy  $PE$  is defined as

$$\begin{aligned} PE &= \frac{1}{2} \int \int \eta^2 dA, \\ &= \frac{1}{2} \int_0^{S^{-1}} \int_{-\pi}^{\pi} \eta^2 r d\theta dr, \end{aligned} \quad (\text{A } 11)$$

where  $S^{-1}$  is the dimensionless radius. Initially  $\eta = -(1/2) \operatorname{sgn} \theta$  and hence the initial potential energy  $IPE = \pi(S^{-1})^2/8$ . The geostrophic interface displacement  $\eta$  is given by (4.3). Squaring  $\eta$ , substituting into (A 11), integrating and using the orthogonality relation between trigonometric functions gives

$$PE = \frac{2}{\pi} \sum_{n=0}^{\infty} \frac{1}{(2n+1)^2} \int_0^{S^{-1}} f_{2n+1}^2 r dr. \quad (\text{A } 12)$$

The kinetic energy  $KE$  of the geostrophic response is

$$KE = \frac{1}{2} \iint |\nabla\eta|^2 dA. \quad (\text{A } 13)$$

While the expression (A 13) could be used to calculate  $KE$ , it proves simpler to derive an alternative expression for  $KE$ . First, substitute the identity

$$\nabla\eta \cdot \nabla\eta = \nabla \cdot (\eta \nabla\eta) - \eta \nabla^2\eta \quad (\text{A } 14)$$

into (A 13) and use Green's theorem to write the first term as an integral of  $\eta \nabla\eta$  around the boundary of the tank. This vanishes owing to the fact that  $\eta = 0$  on  $r = S^{-1}$  (from (4.3)). Hence

$$KE = -\frac{1}{2} \iint \eta \nabla^2\eta dA. \quad (\text{A } 15)$$

But the steady solution satisfies  $\nabla^2\eta - \eta = -(1/2) \text{sgn } \theta$  which, upon substituting into (A 15), and using (A 11) gives

$$\begin{aligned} KE &= -PE + \frac{1}{4} \iint \eta \text{sgn } \theta dA, \\ &= -PE - \frac{2}{\pi} \sum_{n=0}^{\infty} \frac{1}{(2n+1)^2} \int_0^{S^{-1}} f_{2n+1} r dr, \end{aligned} \quad (\text{A } 16)$$

where the result

$$\int_{-\pi}^{\pi} \sin(2n+1)\theta \text{sgn } \theta d\theta = \frac{4}{2n+1} \quad (\text{A } 17)$$

has been used.

The velocity and length scales are the same for a two-layer fluid but now  $H = H_1 H_2 / (H_1 + H_2)$  where  $H_1$  and  $H_2$  are the undisturbed depths of each of the two layers. If, as in the experiments,  $H_1 = H_2 = H^*$  then  $H = H^*/2$ . Thus, the kinetic energy in each layer of the two-layer system, scales as  $KE \sim U^2 \sim g'H \sim g'H^*/2$ . Since there are now two active layers the total kinetic energy scales like  $g'H^*$ . Moreover, the  $PE$  is the same in both two- and one-and-a-half-layer systems. Hence, the expressions and relative behaviour of both the total  $PE$  and  $KE$  are the same in both systems.

## Appendix B. The forcing lengthscale

In the following, the solution for the one-dimensional adjustment problem

$$\frac{d^2\eta}{dx^2} - \eta = -G, \quad (\text{B } 1a)$$

$$\eta(0) = \eta(2S_0^{-1}) = 0, \quad (\text{B } 1b)$$

where the forcing length scale  $r_f$  and the basin radius  $R_0$  have been scaled with  $R$  (see figure 14), is derived in terms of Fourier series, in order to illustrate the role of the initial state  $G(x)$  on the final adjusted state  $\eta(x)$ . The Fourier series expansion of  $\eta$  satisfying the boundary conditions (B1b) is

$$\eta(x) = \sum_{n=1}^{\infty} A_n \sin k_n x, \quad (\text{B } 2)$$

where  $k_n = n\pi/2S_0^{-1}$ . The sine series expansion for the initial state  $G$  is

$$G(x) = \sum_{n=1}^{\infty} G_n \sin k_n x, \quad (\text{B } 3)$$

where

$$G_n = \frac{1}{2S_0^{-1}} \int_0^{2S_0^{-1}} G(x) \sin k_n x \, dx. \quad (\text{B } 4)$$

Equations (B 2) and (B 3) are then substituted into the non-homogeneous Helmholtz equation (B 1a), yielding the coefficients of the solution (B 2)

$$A_n = \frac{G_n}{1 + k_n^2}. \quad (\text{B } 5)$$

The appropriate expansion for the velocity field follows from

$$v(x) = \eta_x = \sum_{n=1}^{\infty} k_n A_n \cos k_n x. \quad (\text{B } 6)$$

Using the definition for the potential ( $PE$ ) and kinetic ( $KE$ ) energies, the total geostrophic energy is given by

$$TGE = \frac{\sum_{n=1}^{\infty} (1 + k_n^2) A_n^2}{\sum_{n=1}^{\infty} G_n^2}, \quad (\text{B } 7)$$

which can be calculated as a function of the initial state  $G(x)$  only.

#### REFERENCES

- ANTENUCCI, J. & IMBERGER, J. 2001 Energetics of long internal gravity waves in large lakes. *Limnol. Oceanogr.* **46**, 1760–1773.
- BENDAT, J. S. & PIERSON, A. G. 2000 *Random Data: Analysis and Measurement Procedures*, 3rd edn. Wiley.
- BOSS, E. & THOMPSON, L. 1995 Energetics of nonlinear geostrophic adjustment. *J. Phys. Oceanogr.* **25**, 1521–1529.
- BOYCE, W. E. & DI PRIMA, R. C. 1992 *Elementary Differential Equations and Boundary Value Problems*, 5th edn. Wiley.
- CSANADY, G. 1967 Large-scale motion in the great lakes. *J. Geophys. Res.* **72**, 4151–4162.
- DORMAN, C. 1987 Possible role of gravity currents in Northern California's coastal summer wind reversals. *J. Geophys. Res.* **92**, 1467–1488.
- GILL, A. E. 1976 Adjustment under gravity in a rotating channel. *J. Fluid Mech.* **77**, 603–621.
- GILL, A. E. 1982 *Atmosphere-Ocean Dynamics*. Academic.
- VAN HEIJST, G. J. F. & SMEED, D. 1986 On the energetics of adjustment problems in stratified rotating fluids. *Ocean Model.* **68**, 1–3.
- HELFRICH, K. R., KUO, A. C. & PRATT, L. J. 1999 Nonlinear Rossby adjustment in a channel. *J. Fluid Mech.* **390**, 187–222.
- HERMAN, G. 1989 The time dependent response of Lake Kinneret to an applied wind stress and hydraulic flow: Advection of suspended matter. *Arch. Hydrobiol.* **115**, 41–57.
- HERMANN, A. J., RHINES, P. B. & JOHNSON, E. R. 1989 Nonlinear Rossby adjustment in a channel: beyond Kelvin waves. *J. Fluid Mech.* **205**, 469–502.
- LAMB, S. H. 1932 *Hydrodynamics*. Dover.
- MARTINSEN, E. & WEBER, J. 1981 Frictional influences on internal Kelvin waves. *Tellus* **33**, 402–410.

- MIDDLETON, J. F. 1987 Energetics of linear geostrophic adjustment. *J. Phys. Oceanogr.* **17**, 735–740.
- OU, H. W. 1986 On the energy conversion during geostrophic adjustment. *J. Phys. Oceanogr.* **16**, 2203–2204.
- ROSSBY, C.-G. A. 1937 On the mutual adjustment of pressure and velocity distributions in certain simple current systems. i. *J. Mar. Res.* **1**, 15–28.
- ROSSBY, C.-G. A. 1938 On the mutual adjustment of pressure and velocity distributions in certain simple current systems. ii. *J. Mar. Res.* **1**, 239–263.
- RUDDICK, B. R. & SHIRTCLIFFE, T. G. L. 1979 Data for double diffusers: physical properties of aqueous salt-sugar solutions. *Deep-Sea Res.* **26**, 775–787.
- SAGGIO, A. & IMBERGER, J. 1998 Internal wave weather in a stratified lake. *Limnol. Oceanogr.* **43**, 1780–1795.
- SERRUYA, S., HOLLAN, E. & BITSCH, B. 1984 Steady winter circulations in Lake Constance and Kinneret driven by wind and main tributaries. *Arch. Hydrobiol.* **1**, 33–110.
- STERN, M. E. & HELFRICH, K. R. 2002 Propagation of a finite-amplitude potential vorticity front along the wall of a stratified fluid. *J. Fluid Mech.* **468**, 179–204.
- STOCKER, R. & IMBERGER, J. 2003 Energy partitioning and horizontal dispersion in the surface layer of a stratified lake. *J. Phys. Oceanogr.* **33**, 512–529.